Dalton Transactions

PAPER

View Article Online
View Journal

Cite this: DOI: 10.1039/c4dt01476f

A simple and convenient approach for preparing core–shell-like silica@nickel species nanoparticles: highly efficient and stable catalyst for the dehydrogenation of 1,2-cyclohexanediol to catechol†

Bao-Hui Chen, Wei Liu, An Li, Ya-Juan Liu and Zi-Sheng Chao*

A simple and convenient approach denoted as gel-deposition–precipitation (G-D–P) for the preparation of core–shell-like silica@nickel species nanoparticles was studied systematically. Core–shell-like silica@nickel species nanoparticles consisted of a Si-rich core and a Ni-rich shell. The G-D–P process included two steps: one was the deposition–precipitation of nickel over the gelled colloidal silica particle, generating core–shell-like silica@nickel species nanoparticles, and the other was the aging period. It was found that the nickel phyllosilicate layer was formed mainly during the aging period and served as the protective cover to resist against aggregation of the nanoparticles, which could be utilized for regulating the dispersion of nickel over the silica@nickel species nanoparticles. In the present paper, the silica@nickel species nanoparticles were used as the catalysts for preparing catechol *via* dehydrogenation of 1,2-cyclohexanediol. Their catalytic activity and long-term stability were compared to those of a catalyst prepared by a conventional deposition–precipitation (D–P) approach. The higher activity and better stability of the title reaction over the silica@nickel species nanoparticles catalyst prepared by G-D–P than those over the catalyst prepared by D–P could be due to the higher dispersion of metallic nickel stabilized by the layers of nickel phyllosilicates. Moreover, it was found that the dehydrogenation of 1,2-cyclohexanediol to catechol was a structurally sensitive reaction.

Received 20th May 2014,
Accepted 28th July 2014

DOI: 10.1039/c4dt01476f

www.rsc.org/dalton

1. Introduction

Utilization of nanosized metal particles or clusters in catalysis is regarded as one of the most important applications of nanomaterials.[1–3] The use of metallic nanomaterial catalysts is tempting due to their high surface areas and small sizes. As is well known, different nanomaterials with given shapes have different facets and distinctive ratios of the amount of atoms on corners and edges to those on facets;[4] it would be in favor of some special catalytic reactions, and could be useful for the design of highly effective and exclusive catalysts.[4,5] Furthermore, with the reduction of the size of catalyst particles to the region of ultimate nanoclusters, some new catalytic properties would be seen, which could not been forecasted by extrapolation of the behavior known for the larger size.[6,7]

However, few metallic nanomaterials are used independently for catalytic reactions because of their low thermal stability, especially under the reaction temperature.[8] Therefore, core–shell metal@oxide nanoparticles have attracted considerable attraction due to their better property of stability.[9] Usually, some oxides with high chemical and thermal stabilities, *e.g.*, SiO_2,[10,11] TiO_2,[12] Al_2O_3,[13] and Cr_2O_3,[14] serve as shells to protect the susceptive metal nanoparticle cores. Among these inert oxides, SiO_2 is the most studied shell candidate because of its outstanding environmental stability and compatibility with other materials, and relative ease in preparation.[15] Herein, taking the core–shell metals@SiO_2 as examples, *e.g.*, Ni@SiO_2 [16] and Au@SiO_2,[10] the nano-sized metal particle cores, *i.e.*, Ni[16] and Au[10] cores, are the catalytically active components, and SiO_2 exists as shells, whose framework acts as nano-sized reaction vessels, providing a stable environment even at high reaction temperatures.[16–18] However, when the core–shell metal@oxide nanomaterials are used as catalysts, a problem should be noticed: the thick and closed protective inert oxide shells lower the active surface area and slow down the diffusions of both reactants and products during the catalytic reaction, although they can protect the susceptive metallic cores.

Comparatively, core–shell oxide@metal nanoparticles can be regarded as a kind of highly dispersed oxide supported metal catalyst. Taking the core–shell SiO_2@Ni nanoparticles as

College of Chemistry and Chemical Engineering, State Key Laboratory of Chemo/Biosensing and Chemometrics, Hunan University, Changsha, 410082, China. E-mail: zschao@yahoo.com; Fax: +86-731-88713257; Tel: +86-731-88713257

† Electronic supplementary information (ESI) available. See DOI: 10.1039/c4dt01476f

an example, silica cores can act as the support, and the fine nickel nanoparticles are deposited over the surface of cores as the shells. Surprisingly, few works have been reported on the core–shell oxide@metal nanomaterials and their applications in the catalysis field[13,19] relative to those on the core–shell metal@oxide nanoparticles.[13,16–18] It is probably due to the fact that it is always a challenge to keep the fine metal nanoparticles loaded from aggregation and sintering during the application of catalytic reactions, if they are directly deposited over the nano-sized cores.

Core–shell nanomaterials are fabricated usually using a two-step approach.[20] The first step is the synthesis of colloidal nanoparticle cores in the presence of organic capping agents, *i.e.*, polymers or surfactants, which keep the nanoparticles from aggregation in solution, and the second one is the growth of shells deposited on the cores. The main issues associated with this method are the high cost, complex operation, and low production efficiency, which restricts its broader industrial applications.

Highly concentrated colloidal silica solutions that are used in industrial applications since the 1940s are made of discrete particles of amorphous silica of relatively uniform particle size from *ca.* 5 to 100 nm.[21] They seem to be an economic source of silica cores for the fabrication of core–shell silica@metal nanoparticles. Moreover, the formation of nickel phyllosilicate is observed in core–shell Ni@SiO_2,[16] which is generated due to the interaction between silica and nickel compounds. It has been found that, metal phyllosilicates can be used to stabilize nanoparticles due to its high thermal stability and reduction susceptibility.[16,22]

The sol–gel[23] and deposition–precipitation (D–P)[24] methods are two important approaches for the preparation of dispersed metal catalysts. The sol–gel approach possesses the advantage in stabilizing the active phase supported;[25] the deposition–precipitation (D–P) method exhibits many advantages in the synthesis of high metal loaded catalysts possessing small metal particles with a rather narrow size distribution.[24] In this work, by combining the merits of the sol–gel and deposition–precipitation methods, we report a strategy for preparing core–shell-like silica@nickel species nanoparticles by a simple and convenient method named gel-deposition–precipitation (G-D–P). This process is composed of the first gelation (G) of the colloidal silica solution, followed by the deposition–precipitation (D–P) of nickel over the gelled silica nanoparticles. This method uses the colloidal silica particles directly as the source of the silica cores, and nickel phyllosilicates as the protective coat to stabilize the nanoparticles, which demonstrates the characteristics of low cost, small operation complexity, and high production efficiency. In addition, interestingly, the dispersion degree of nickel over the core–shell-like silica@nickel species nanoparticles can be controlled easily by regulating the preparation (G-D–P) time.

Catechol has wide applications in many fields, *e.g.*, medicines, pesticides, dyes, spices, and chemical auxiliary agents.[26,27] The current industrial production scheme for catechol is the hydroxylation of phenol with hydrogen peroxide.[28] However, this route suffers from some drawbacks, *i.e.*, low conversion (theoretical conversion = 33.3%[28]) and selectivity (typically <60%[28]), and a rigorous and complex separation route.[29] Comparatively, dehydrogenation of 1,2-cyclohexanediol provides another promising reaction pathway for preparing catechol because of its high conversion and selectivity, and easy separation procedures.[29] This pathway is derived from cyclohexene, which is commercial available from several companies, *e.g.*, Asahi Chemical.[30] The starting material 1,2-cyclohexanediol can be achieved by two different strategies: one is the one-pot epoxidation and hydrolysis (dihydroxylation) of cyclohexene (see ESI Scheme 1S A†), *e.g.*, *ca.* 98% yield of 1,2-cyclohexanediol was obtained using a resin-supported sulfonic acid catalyst.[31] The other one is the first oxidation of cyclohexene, forming cyclohexene oxide,[30,32–34] followed by its hydration to obtain 1, 2-cyclohexanediol (see Scheme 1S B†).[35,36] This strategy, typically, has a yield of *ca.* 95% on the basis of cyclohexane.[36,37] It has been reported that, alkali metal modified Ni-based catalysts are active for preparing catechol by the dehydrogenation of 1,2-cyclohexanediol,[27,29,38,39] *e.g.*, over a Na-doped HZSM-5 supported Ni catalyst,[29] 95.8% selectivity of catechol at a 99.9% of conversion was obtained, and the high performance could be retained for as long as 40 h of on-stream reaction. In the present paper, preparation of catechol *via* dehydrogenation of 1,2-cyclohexanediol was used as the model reaction for studying the core–shell-like silica@nickel species nanoparticles catalysts prepared by G-D–P method, and their catalytic properties and long-term stability were compared to those of a catalyst prepared by a conventional deposition–precipitation (D–P) approach.

2. Experimental section

2.1. Catalysts preparation

Nickel nitrate (A.R; Xilong Chemical Co., China), urea (A.R; Kemiou Chemical Co., China) and colloidal silica solution (commercial grade, $SiO_2 \cdot nH_2O$, 30.0 wt%, Na_2O type, pH ≈ 10) were employed to prepare the core–shell-like silica@nickel species nanoparticles. The colloidal silica solution was first dispersed into a 7.5 wt% aqueous solution of urea, with a colloidal silica solution/urea = 1 in weight ratio, at room temperature with stirring. Then, a calculated amount of 2.5 wt% aqueous solution of nickel nitrate salt was added into this homogeneous solution. The resultant mixture was heated to 95 °C within 20 min, and stirred for a chosen time (0.17–48 h) at this temperature point, when the colloidal silica solution was gelled and nickel nitrate salt was deposited-precipitated. This process is called the gel-deposition–precipitation (G-D–P) approach by us. After it cooled to room temperature, the so-prepared mixture was recovered by a separation process, washed repeatedly with de-ionized water and dried at 80 °C for 12 h. The resultant powder was further calcined in air at 450 °C for 4 h, forming the core–shell-like silica@nickel species nanoparticles, denoted as Si–*X*Ni(*Y*). Herein, *X* refers to the theoretical nickel weight loading (named as Ni_T, wt%)

when overall the nickel nitrate and colloidal silica particles in solution have been deposited–precipitated/and gelled, and its value equals to 10–50 (wt%); *Y* refers to the G-D–P time expressed in hours, and its value equals to 0.17–48 (h). For example, Si–20Ni(4) represents the catalyst that was prepared according to a 20 wt% of theoretical loading of Ni in catalyst and *via* 4 hours of G-D–P. Moreover, to figure out the effect of calcination, the catalysts prepared *via* the above procedure but without the step of calcination at 450 °C were also employed in the studies, and these catalysts were defined as uncalcined Si–*X*Ni(*Y*).

However, the actual Ni and silica weight loadings remarkably depend on the G-D–P time. Thus, after the G-D–P procedure, the actual loadings of Ni and silica, namely, Ni_A and $Silica_A$ respectively, can be lower than the theoretical loadings of Ni and silica, namely, Ni_T and $Silica_T$ respectively. In this paper, the Ni_A and $Silica_A$ values were determined by atomic absorption spectroscopy (AAS, see section 2.2). Moreover, the differences between the Ni_T and Ni_A values, and between the $Silica_T$ and $Silica_A$ values, were evaluated by the yields of Ni (Y_{Ni}) and silica (Y_{Silica}) loadings, respectively, which refer also to the recovery rates of Ni and silica, respectively, after the G-D–P procedure. The calculations of Ni_T, Ni_A, $Silica_T$, $Silica_A$, Y_{Ni} and Y_{Silica} values are expressed as follows:

$$Ni_T(wt\%) = \frac{W_{Ni,T}}{W_{Ni,T} + W_{Silica,T}} \times 100\%$$

$$Silica_T(wt\%) = \frac{W_{Silica,\,T}}{W_{Ni,\,T} + W_{Silica,\,T}} \times 100\%$$

$$Ni_A(wt\%) = \frac{W_{Ni,\,A}}{W_{catalyst,\,A}} \times 100\%$$

$$Silica_A(wt\%) = \frac{W_{Silica,\,A}}{W_{catalyst,\,A}} \times 100\%$$

$$Y_{Ni}(\%) = \frac{Ni_A}{Ni_T} \times 100\%$$

$$Y_{Silica}(\%) = \frac{Silica_A}{Silica_T} \times 100\%$$

where $W_{Ni,T}$ refers to the weight of Ni in the solution of nickel nitrate used for the preparation of catalyst; $W_{Silica,T}$ is the weight of silica in the colloidal silica solution employed in the preparation of the catalyst; $W_{Ni,A}$ and $W_{Silica,A}$ are the actual weights of Ni and silica, respectively, determined by AAS, in the catalyst; and $W_{catalyst}$ stands for the weight of the catalyst used in the AAS determination.

However, some of the colloidal silica solution was directly dried at 80 °C and calcined in air at 450 °C for 4 h to obtain the SiO_2 sample. Moreover, the obtained SiO_2 sample was utilized for preparing the Si–20Ni(4)–DP catalyst by a conventional deposition–precipitation (D–P) approach. The SiO_2 sample obtained above (sieved to 100–120 mesh) were first dispersed into a 7.5 wt% aqueous solution of urea with a liquid–solid weight ratio of 12.5 at room temperature with stirring. Then, a calculated amount of 2.5 wt% aqueous solution of nickel nitrate salt was added, and the resultant mixture was heated to 95 °C, and stirred for an additional 4 h. After it cooled to the room temperature, the precipitate was recovered by separation, washed repeatedly with de-ionized water and dried at 80 °C for 12 h. Finally, the resultant powders were calcined in air at 450 °C for 4 h, generating the nickel loaded silica catalyst, which was denoted as Si–20Ni(4)–DP, where the content of Ni in the catalyst is 20 wt%, and the preparation (D–P) time is 4 h.

According to a previous paper,[29] the 2Na/Si–*X*Ni(*Y*) and 2Na/Si–20Ni(4)–DP catalysts were prepared by a impregnation method using the prepared Si–*X*Ni(*Y*) and Si–20Ni(4)–DP catalysts above as the support and calculated amount of aqueous solution of sodium sulfate to provide the precursor salt, where the Na content was uniformly 2 wt% in catalysts.

2.2. Catalysts characterization

Fourier transform infrared (FT-IR) spectroscopy in KBr was recorded by utilizing a Varian 3100 spectrometer. Each spectrum was recorded as a result of the accumulation of 32 scans at a resolution of 2 cm^{-1}. X-ray diffraction (XRD) was performed using the Bruker D8-Advance X-ray diffraction equipment, under the following conditions: Cu target K_α ray (λ = 1.54187 Å); scanning voltage, 40 kV; scanning current, 40 mA; scanning speed, 0.5 s, scanning step, 0.02°. N_2-absorption/desorption isotherm was carried out on a Quantachrome Autosorb-1 instrument at liquid–N_2 temperature. The BET method was used to calculate the specific surface area, and the average pore size was determined by the Barrett–Joyner–Halenda (BJH) method. Field-emission scanning electron microscopy (FE-SEM) was performed with a JSM 6700F scanning electron microscope. Transmission electron microscopy (TEM) and high-angle annular dark-field scanning transmission electron microscopy (HAADF-STEM) were performed with a Tecnai F20 electron microscope (Philips Analytical) with an EDAX-Genesis type energy dispersive X-ray spectrometer (EDS) operated at an acceleration voltage of 200 kV. Temperature-programmed oxidation (O_2-TPO) and temperature-programmed desorption of H_2 (H_2-TPD) were performed using a Quantachrome Autosorb-1 instrument equipped with a thermal conductivity detector (TCD). The reduction extent of nickel was estimated by O_2-TPO, and the number of surface nickel atoms available was assessed by H_2-TPD.[40] The dispersion degree of metallic nickel was identified according to the formula for the calculation reported previously,[40] which assumed an adsorption stoichiometry of one hydrogen atom per surface metallic nickel atom. Flame atomic absorption spectrometry (AAS) performed by a Varian AA240 apparatus was utilized to determine the elemental compositions of the catalyst. X-ray photoelectron spectroscopy (XPS) was performed by a PHI Quantum 2000 XPS system with a monochromatic Al Kα source and a charge neutralizer. The binding energy (B.E.) was referenced to the C 1s peak at 284.8 eV for the surface adventitious carbon.

2.3. Dehydrogenation of 1,2-cyclohexanediol

The reaction was performed by using a fixed-bed, flow-type stainless reactor (33 cm × 1.5 cm × 0.8 cm), which was mounted in a tubular electric heater. For a typical reaction, first, *ca.* 0.5 g catalyst was filled in the middle of the reactor, and the upper space of the catalyst bed in the reactor was filled with inert quartz granulates (20–40 mesh). Before the reaction, the temperature was increased to 450 °C in 60 min, and then a flow of H_2 was introduced from the upper of reactor to activate the catalyst. After the H_2 activation for 4 h, the temperature was decreased to 320 °C. Then, the reactant, a 10 wt% 1,2-cyclohexanediol aqueous solution, was pumped into the reactor at a constant liquid hourly space velocity (LHSV) of 1.43 h^{-1}, while the flow of H_2 was kept to provide a reduction environment and constant total pressure of 0.1 MPa. The effluent from the bottom of reactor was passed through a gas–liquid separator cooled by ice-water.

The catalytic rate for the dehydrogenation of 1,2-cyclohexanediol was measured under reaction conditions as follows: catalyst weight was in the range of 10–20 mg, total pressure was 0.1 MPa, reduction temperature was 450 °C, reaction temperatures was 250 °C, and LHSV was 160 h^{-1}. Quantities of catalyst filled in the reactor referred to the same amount of surface metallic nickel (= 9.9 × 10^{18} metallic nickel atoms). The reaction conversion was controlled in the range of 4%–13% to ensure that the experimental results obtained are in the region of intrinsic kinetics. Moreover, transport artifacts were eliminated by experimental method, leading to undetectable variations in catalytic reaction rates or selectivities.

The qualitative and quantitative analyses of the liquid products mixture were carried out with a Varian Saturn 2200/CP 3800 GC/MS spectrometer, equipped with a flame ionization detector (FID) and two CP-Wax 52CB fused silica capillary columns (15 m × 0.32 mm). It was identified that,[29] in addition to the aimed product catechol, the byproducts cyclopentanone, cyclopentanol, phenol, cyclohexanone, cyclohexanol, *o*-hydroxyl-cyclohexanone, and, in some cases, the unconverted 1,2-cyclohexanediol, were also present in the liquid products mixture. The quantitative analysis of the gas products mixture was carried out with a PE Clarus 500 GC, which was equipped with a thermal conductivity detector (TCD) and a HAYESEP DB 100/120 packed column (30′ × 1/8″ × 0.85″ SS). The conversion of 1,2-cyclohexanediol (χ) and selectivity towards product (S_i) were defined as follows:

$$\chi\,(\mathrm{mol}\%) = \frac{X_0 - X_1}{X_0} \times 100\%$$

$$S_i\,(\mathrm{mol}\%) = \frac{Y_i}{\sum_{i=1}^{n} Y_i} \times 100\%$$

where X_0 and X_1 refer to the initial and final moles of 1,2-cyclohexanediol, respectively; Y_i indicated the mole of component i in the products mixture.

3. Results

3.1. Gel-deposition–precipitation (G-D–P) process

Fig. 1a shows the changes in the actual Ni and silica loadings (Ni_A and $Silica_A$, respectively) and yields of Ni and silica loadings (Y_{Ni} and Y_{Silica}, respectively) over the Si–XNi(4) catalysts, as a function of theoretical Ni loading (Ni_T). These catalysts are prepared uniformly with the same G-D–P time = 4 h. At the Ni_T value below 20 wt%, the Y_{Ni} value retains a high value above 99.9%, which indicates that almost all of the Ni species in the solution have been deposited at relatively low Ni_T

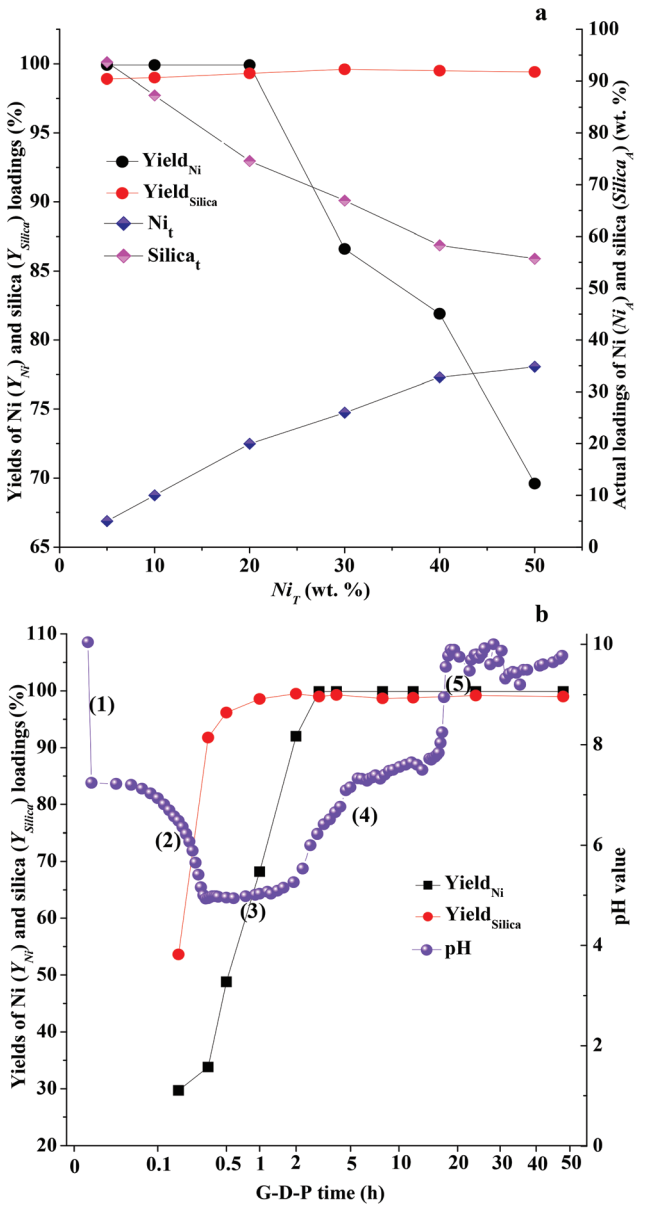

Fig. 1 (a) Changes of actual Ni and silica loadings (Ni_A and $Silica_A$, respectively) and yields of Ni and silica loadings (Y_{Ni} and Y_{Silica}, respectively) over Si–XNi(4) catalysts as a function of theoretical Ni loading (Ni_T). (b) Changes of yields of Ni and silica loadings (Y_{Ni} and Y_{Silica}, respectively) and pH value over Si–20Ni(*Y*) catalysts prepared at various G-D–P time *Y* (*Y* = 0.17–48 h).

values. However, it is found that, when the Ni_T value is in excess of 20 wt%, the Y_{Ni} value decreases steeply to lower values. This result suggests the incomplete deposition of the nickel species in the solution at the relatively high Ni_T values. Comparatively, the actual Ni loading (Ni_A) displays a monotonic increase (from 5 to 33 wt%) with increasing the Ni_T value. The result that the yield of Ni loading (Y_{Ni}) decreases with the increase of the Ni_T value at the relatively high Ni_T values can be explained by the fact that the higher the nickel concentration in solution, the more OH^- ions are required for the deposition–precipitation of Ni. However, during the deposition–precipitation of Ni, the generation of OH^- ions is limited by the pyrolysis rate of urea.[41] Thus, at the relatively high Ni_T values, the nickel species in the solution cannot be totally precipitated after only 4 h G-D–P. Moreover, although the actual silica loading ($Silica_A$) decreases with increasing the Ni_T value, the Y_{Silica} value always demonstrates a high value above 98.5%. This result indicates that almost all the colloidal silica solutions have been gelled after 4 h of G-D–P.

The changes of yields of Ni and silica loadings (Y_{Ni} and Y_{Silica}, respectively) of Si–20Ni(*Y*) catalysts and pH value as a function of G-D–P time are shown in Fig. 1b. These catalysts are prepared by employing the same nickel concentration in solutions, which corresponds to a theoretical Ni loading (Ni_T) = 20 wt%. One can see that, with increasing the G-D–P time, the Y_{Ni} and Y_{Silica} values first show a steep increase, attaining 99.9% and 99.5% at the G-D–P time equal to 3 and 2 h, respectively, and then maintaining these high values when the G-D–P time is above these time values. Thus, it can be concluded that, after 3 h of G-D–P, almost all the colloidal silica solution and Ni species in the solution have been gelled/and deposited–precipitated, and beyond this time, the catalyst is aging. Nevertheless, it is found that, the gelation of colloidal silica solution is faster, obviously, than the deposition–precipitation of Ni. For instance, 56% and 91.8% of colloidal silica solutions have been gelled at 0.17 and 0.33 h of G-D–P, respectively, when only 29.7% and 33.8% of Ni have been deposited–precipitated, respectively. This result indicates that, during the G-D–P procedure, generally, the colloidal silica solution is gelled firstly; then, the nickel is deposited–precipitated gradually over the surface of gelled silica support.

Moreover, the variation of the pH value depended on the variation of OH^- ions in the solution as a function of G-D–P time is also present in Fig. 1b. The OH^- ions in the solution are composed of two groups. One is the primary presence of OH^- ions owing to the fact that sodium hydroxide is employed as stabilizer in the colloidal silica solution, which are defined as free OH^- ions. The other group is generated OH^- ions due to the hydrolysis of urea during the G-D–P. These OH^- ions can be consumed during the deposition–precipitation of Ni over the silica support. In this figure, the variation of the pH value is divided into five stages: (1) the pH value decreases instantly from *ca.* 10 to 8 after the addition of nickel nitrate into the mixture of urea and colloidal silica solution, and it is related to the consumption of free OH^- ions in the colloidal silica solution with the precipitation of Ni; (2) from the ending of stage (1) to 0.4 h of G-D–P, the pH value decreases quickly; (3) then, a plain stage (pH value = *ca.* 5) is formed from 0.4 to 2 h of G-D–P; (4) from 2 to 16 h of G-D–P, the pH value increases at a relatively mild speed from *ca.* 5 to 8; (5) the pH value increases abruptly from *ca.* 8 to 10, and then fluctuates around this high value, forming a plain stage at pH value = *ca.* 10. Undoubtedly, these variations in pH values are associated with some specific chemical reactions, *e.g.*, the precipitation of Ni and some other reactions during aging of the catalyst, which will be discussed later as a key.

3.2. Catalysts characterizations

Fig. 2 shows the FT-IR spectra of SiO_2, uncalcined Si–*X*Ni(4), Si–*X*Ni(4), and Si–20Ni(4)–DP catalysts. For the absorption bands of pristine SiO_2 (Curve 2 a-i), the bands at *ca.* 478, 801, 964, 1118, 1280 cm^{-1} can be associated with the rocking (R) and bending (B) vibrational modes, the four-fold strained structural ring, as well as the symmetric stretching (AS_1) and coupled disorder induced (AS_2) modes, respectively;[42,43] and the absorptions at *ca.* 3445, 3652, and 3739 cm^{-1} are assigned to the H-bonded Si–OH in chain (O–H stretching), stretching mode of OH groups expect for isolated and terminal OH, and isolated surface silanols (O–H stretching), respectively.[42] Both nickel hydroxide and nickel phyllosilicate can be formed by basification of the nickel salt solution.[24] For uncalcined Si–10Ni(4) (Curve 2 a-ii), three bands at 666, 1058, and 3640 cm^{-1} are present, which are related to the tetrahedral Si–O mode, Si–O stretching, and ν_{OH} vibration, respectively, of 1 : 1 nickel phyllosilicate ($Si_2Ni_3O_5(OH)_4$, also called Ni–lizardite or nepouite).[24,44,45] These bands are present in all of the uncalcined Si–*X*Ni(4) catalysts, and increase in strength with increasing the Ni loading (Curve 2 a-ii to iv, in order). However, the band at *ca.* 637 cm^{-1}, a characteristic band of nickel hydroxide,[24] only can been seen in Curve 2 a-iii and iv. This result shows that, the presence of the Ni(II) phase in the uncalcined Si–*X*Ni(4) catalysts is mainly 1 : 1 nickel phyllosilicate at relatively low Ni loading, and a mixture of 1 : 1 nickel phyllosilicate and nickel hydroxide at relatively high Ni loading. Moreover, the wide band at *ca.* 3313 cm^{-1} indicates the hydrogen-bonded OH bonds of water.[46,47] Note that the band at *ca.* 900 cm^{-1} is always seen over the ill-crystallized nickel phyllosilicate.[24] Furthermore, it should be noticed that, the band at *ca.* 3640 cm^{-1} at high Ni loading (Curve 2 a-iii and iv) is probably an integrated absorption, which is ascribed to the surface hydroxyls of the nickel hydroxide and nickel phyllosilicate mixture, because both of them have a similar absorption of ν_{OH} vibration in this absorption interval.[24]

Compared to uncalcined Si–*X*Ni(4), for Si–*X*Ni(4) (see Fig. 2b); (1) the disappearance of the band at *ca.* 637 cm^{-1} indicates the decomposition of nickel hydroxide; (2) the band at *ca.* 3640 cm^{-1} disappears, and a new band emerges at *ca.* 3626 cm^{-1}, which is a characteristic band of 2 : 1 nickel phyllosilicate ($Si_4Ni_3O_{10}(OH)_2$, also called Ni–talc or willemseite);[24] (3) the bands at *ca.* 1058 and 666 cm^{-1} shift to the higher wavenumbers at *ca.* 1034 and 671 cm^{-1}, respectively, and the latter two wavenumbers are assigned to 2 : 1 nickel

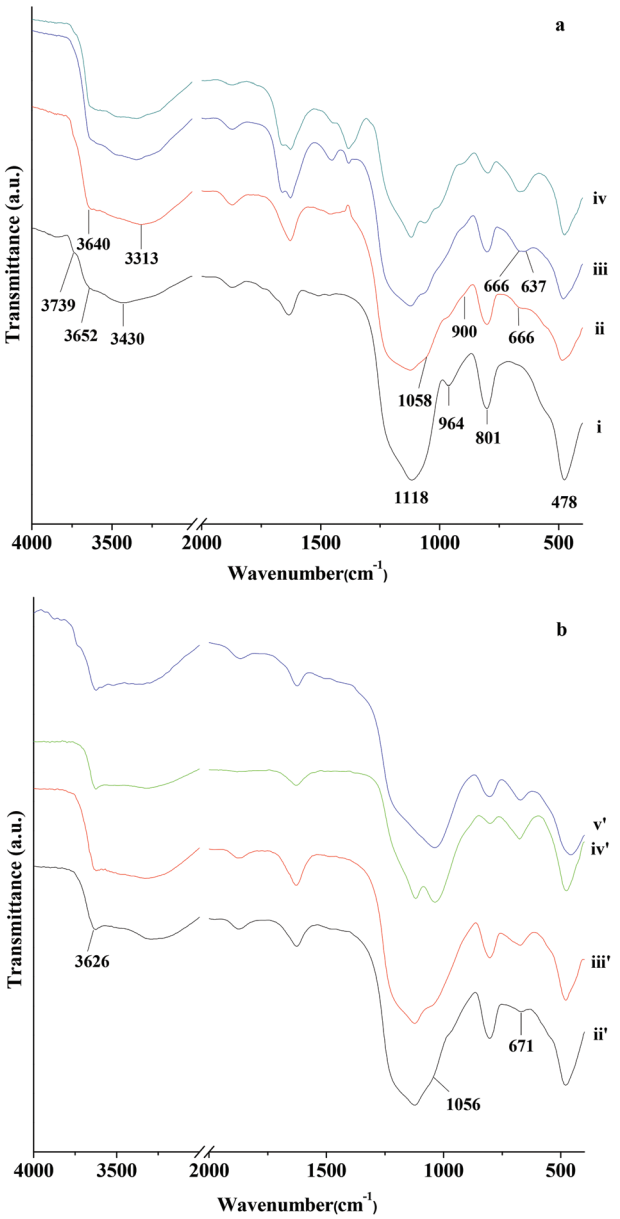

Fig. 2 (a) FT-IR spectra of (i) SiO_2 and uncalcined Si–*X*Ni(4) catalysts, *X* = (ii) 10, (iii) 20 and (iv) 50, respectively. (b) FT-IR spectra of Si–*X*Ni(4) catalysts, *X* = (ii′) 10, (iii′) 20 and (iv′) 50, respectively; and (v′) Si–20Ni(4)–DP.

phyllosilicate;[24] (4) the band at *ca.* 900 cm^{-1} disappears, which demonstrates that 2 : 1 nickel phyllosilicates in the Si–*X*Ni(4) catalyst have relatively good crystallinity.[24] It should be noted that, no obvious bands related to nickel oxides, which should be formed with the decomposition of nickel hydroxides, are observed in Si–*X*Ni(4). This finding can be due to the fact that, the bands of nickel oxides overlap with those of SiO_2, which makes the assignment difficult. According to the results above, during the calcination, nickel hydroxides are decomposed; moreover, a 1 : 1 nickel phyllosilicate transforms into 2 : 1 nickel phyllosilicate. Moreover, the FT-IR spectrum of Si–20Ni(4)–DP is present in Fig. 2b–v′, which shows the stronger bands at *ca.* 666 and 3626 cm^{-1} relative to that of Si–20Ni(4). This result suggests that, more nickel phyllosilicates are present over the Si–20Ni(4)–DP catalyst prepared by the conventional D–P method, than the Si–20Ni(4) catalyst prepared by the G-D–P method depicted in this work.

Fig. 3 shows the FT-IR spectra of uncalcined Si–20Ni(*Y*) and Si–20Ni(*Y*) catalysts. For the uncalcined Si–20Ni(*Y*) catalysts (see Fig. 3a), at a low G-D–P time below 2 h, the absorption bands at *ca.* 639 and 3640 cm^{-1} are attributed to nickel hydroxide.[24] With increasing the G-D–P time up to 4 h, the band at *ca.* 666 cm^{-1}, characteristic of 1 : 1 nickel phyllosilicate,[24] emerges and increases in strength with increasing the G-D–P time further. Comparatively, first, the band at *ca.* 639 cm^{-1}

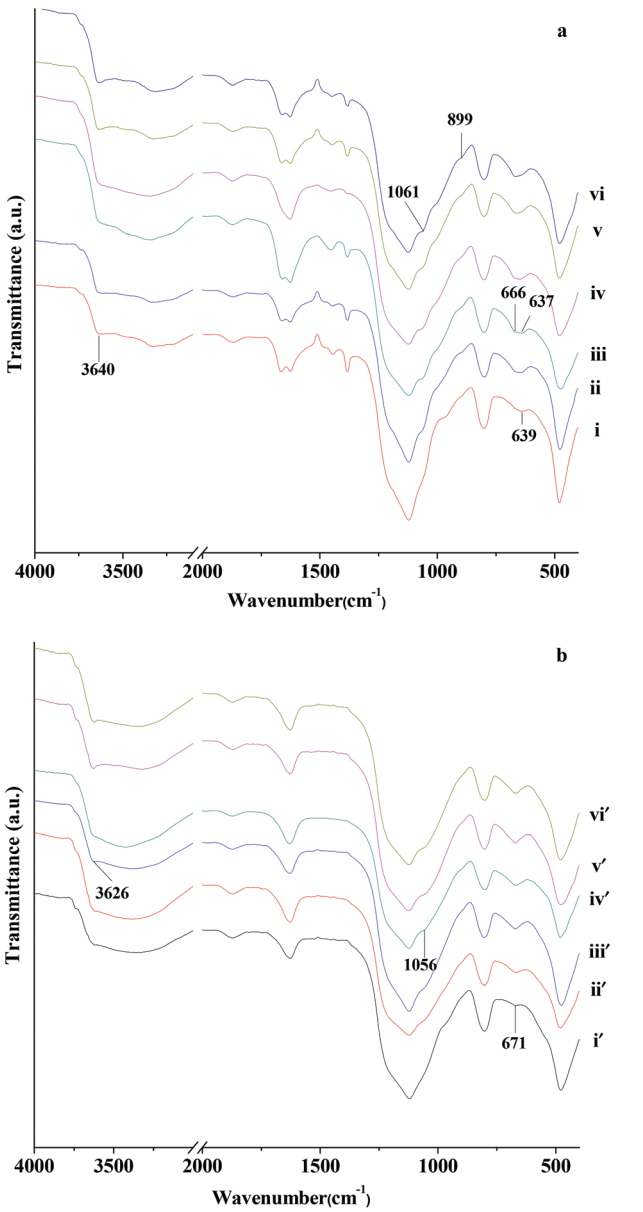

Fig. 3 (a) FT-IR spectra of uncalcined Si–20Ni(*Y*) catalysts, *Y* = (i) 1, (ii) 2, (iii) 4, (iv) 8, (v) 12 and (vi) 24, respectively. (b) FT-IR spectra of Si–20Ni (*Y*) catalysts, *Y* = (i′) 1, (ii′) 2, (iii′) 4, (iv′) 8, (v′) 12 and (vi′) 24, respectively.

increases in strength with increasing the G-D–P time, and attains its maximum at 4 h of G-D–P, followed by a decrease with the further increased G-D–P time. This result indicates that, at a relatively low G-D–P time, nickel hydroxides exhibit in the uncalcined Si–20Ni(*Y*) catalysts as the main form of the Ni(II) phase; however, they transform gradually into 1 : 1 nickel phyllosilicates with the increase in G-D–P time.

After the calcination procedure (see Fig. 3b), the disappeared absorption at *ca.* 637 cm^{-1} suggests the decomposition of nickel hydroxide, as discussed above (see Fig. 2b). Moreover, the absorption bands at 3640 and 1061 cm^{-1} shift to lower wavenumbers at 3626 and 1056 cm^{-1}, respectively, indicating the transformation of 1 : 1 nickel phyllosilicate into 2 : 1 nickel phyllosilicate; moreover, the band at *ca.* 899 cm^{-1} disappears, which is associated with the improvement of the crystallinity of the nickel phyllosilicate.[24]

Fig. 4 shows the XRD patterns of SiO_2, Si–*X*Ni(4), Si–20Ni(*Y*), and Si–20Ni(4)–DP catalysts. For SiO_2, only a broad and diffuse diffraction peak at 2θ = *ca.* 21.7° is seen. This peak is related to the typical amorphous character of the SiO_2 vitreous matrix.[46,48] After the loading of Ni, as can be observed in curve ii to iv that, another set of dispersed reflections at 2θ = *ca.* 28.6°, 34.5°, 60.7°, in addition to the broad diffraction peak of silica, whose strength increase with the Ni loading, are also observed in XRD. This phenomenon indicates the generation of 2 : 1 nickel phyllosilicate, combined with the IR analyses above.[24,44] Moreover, the reflections with respect to NiO at 2θ = *ca.* 37.1°, 43.2°, 62.8° can also be indistinctly identified, when the Ni loading is above 20 wt% (Curve iv). NiO can be generated by the decomposition of nickel hydroxide upon calcination. These results above indicate that, at relatively low Ni loading, the presence of the Ni(II) phase is mainly nickel phyllosilicate, whereas a mixture of nickel phyllosilicate and nickel hydroxide exists at relatively high Ni loading. This conclusion is in agreement with the IR results above.

For Si–20Ni(*Y*), with increasing the G-D–P time (Curve v, ii, vi and vii, in order), the intensities of the diffaction peaks related to 2 : 1 nickel phyllosilicate increase obviously. This finding can be due to the transformation from nickel hydroxide into nickel phyllosilicate in the aging stage, also in line with our FT-IR analyses in Fig. 3. Moreover, the diffusion property of the diffraction reflections of nickel phyllosilicate and NiO suggests that, the nickel species have significantly small particle sizes, and also, are highly dispersed over the silica support.

Furthermore, comparing the XRD pattern of Si–20Ni(4) (Curve iii) with that of Si–20Ni(4)–DP (Curve viii), the diffraction peaks associated with nickel phyllosilicate in the former catalyst is obviously weaker than those in the latter one. This finding shows that more nickel phyllosilicates are present over Si–20Ni(4)–DP than over Si–20Ni(4), consistent with the above IR results (see Fig. 2b).

Fig. 5 shows the N_2-adsorption/desorption isotherms of SiO_2, Si–*X*Ni(4), Si–20Ni(*Y*) and Si–20Ni(4)–DP catalysts. Firstly, all of the isotherms exhibit obvious hysteresis loops at P/P_o > 0.4, demonstrating the presence of mesopores.[49] The beginning of the desorption branch at P/P_o = *ca.* 0.4 is intrinsic to the use of nitrogen as a result of the instability of the meniscus of the condensed nitrogen within the capillary pores.[50–52] In the isotherm of pristine SiO_2, a relatively unobvious hysteresis loop belonging to type H3 or H4 is observed, suggesting complex and irregular shapes, *e.g.*, slit-like pores with uniform

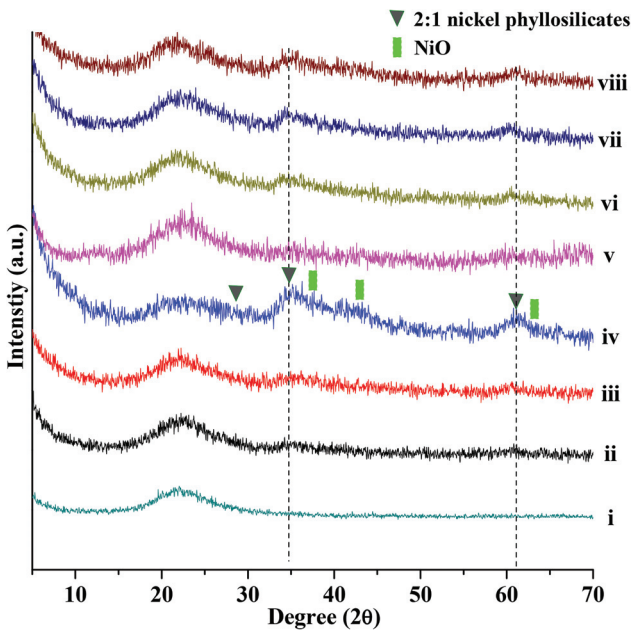

Fig. 4 XRD patterns of (i) SiO_2; Si–*X*Ni(4), *X* = (ii) 10, (iii) 20 and (iv) 50, respectively, Si–20Ni(*Y*), *Y* = (v) 2, (vi) 12 and (vii) 24, respectively, and (viii) Si–20Ni(4)–DP.

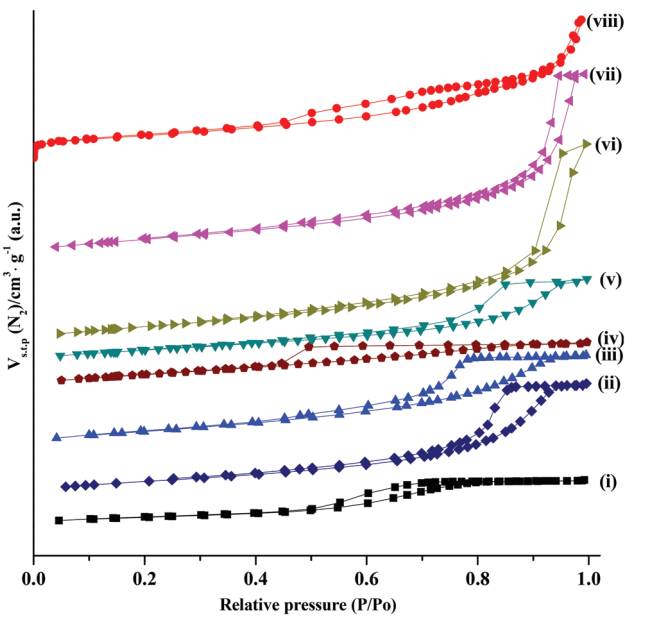

Fig. 5 N_2-adsorption/desorption isotherms of (i) SiO_2; Si–*X*Ni(4), *X* = (ii) 10, (iii) 20, and (iv) 50, respectively, Si–20Ni(*Y*), *Y* = (v) 2, (vi) 12 and (vii) 24, respectively, and (viii) Si–20Ni(4)–DP.

size.[53] Frequently, the H3 and H4 type loops are formed by the aggregation or agglomeration of plates or edged particles like cubes.[54] For Si–*X*Ni(4) catalysts, the isotherm of Si–10Ni(4) (Curve ii) resembles the type H2 hysteresis loop, probably associated with the ink bottle-shaped pore structure. However, when the loading of Ni increases, the hysteresis loop first elevates in magnitude (Si–20Ni(4), Curve iii) because of the increase in the formation of mesoporosity by Ni loading, and then, it is followed by an obvious decrease in magnitude (Si–50Ni(4), curve iv), probably due to the aggregation or agglomeration of the nickel species particles at high Ni loading.

For the Si–20Ni(*Y*) catalysts, with increasing the G-D–P time, the hysteresis loops of the isotherms change from H2-like type at the G-D–P time below 4 h (Curve v and iii) to H1-like type at the D–P-G time in excess of 4 h (Curve vi and vii). The H1 type hysteresis loop is associated with a typical cylindrical-shape pore structure,[54] which is formed by aggregates (consolidated) or agglomerates (unconsolidated) of spheroidal particles. Moreover, the isotherm of Si–20Ni(4)–DP is present in curve viii, exhibiting the similar H4 type hysteresis loop to SiO_2, although its hysteresis loop is obviously bigger than that of SiO_2 in magnitude.

The texture properties of these catalysts, containing specific surface area, total pore volume and average pore size, are summarized in Table 1. For the Si–*X*Ni(4) catalysts, with the increase of Ni loading, the total pore volume and average pore size decrease monotonically (from 0.579 ml g^{-1} and 6.3 nm for Si–10Ni(4) to 0.267 ml g^{-1} and 2.5 nm for Si–50Ni(4), respectively). This result can be caused by the probable partial occupation of silica channels by fine particles of Ni species. However, the specific surface area increases first from 250 m^2 g^{-1} for Si–10Ni(4), to 277 m^2 g^{-1} for Si–20Ni(4), due to the generation of mesoporosity with the doping of Ni, and then, it is followed by a decrease (to 259 m^2 g^{-1} for Si–50Ni(4)), probably ascribed to the aggregation or agglomeration of the Ni species particles at high Ni loading. For the Si–20Ni(*Y*) catalysts, with the increase of G-D–P time, the specific surface area and average pore size increase uniformly (to ~298 m^2 g^{-1} and ~2.9 nm, respectively). The total pore volume increases firstly from 0.449 ml g^{-1} for Si–20Ni(2) to 1.003 ml g^{-1} for Si–20Ni(12), and then, it decreases slightly to 0.920 ml g^{-1} for Si–20Ni(24). These results above can be due to the transformation from nickel hydroxide to nickel phyllosilicate during the aging stage. Moreover, Si–20Ni(4)–DP presents the bigger specific surface area, average pore size, and total pore volume, relative to the SiO_2 support, due to the loading of Ni. Comparing the texture properties of Si–20Ni(4)–DP with those of Si–20Ni(4), the former catalyst exhibits the bigger average pore size and total pore volume, but lower specific surface area, than the latter one.

Table 1 Textural properties, dispersions of metallic nickel, and turnover frequencies of various catalysts

Catalyst	S_{BET} (m^2 g^{-1})	$V_{pore,t}$ (cm^3 g^{-1})	D_{ave} (nm)	Ni_{dis} (%)	TOF_{ini} [a] (h^{-1})
SiO_2	139	0.240	5.7	—	—
Si–10Ni(4)	250	0.579	6.3	20.7	—
Si–20Ni(4)	277	0.484	2.6	10.7	0.22
Si–50Ni(4)	259	0.267	2.5	7.0	—
Si–20Ni(2)	241	0.449	2.0	11.0	0.23
Si–20Ni(12)	298	1.003	2.6	20.9	0.37
Si–20Ni(24)	298	0.920	2.9	26.6	0.45
Si–20Ni(4)–DP	266	0.671	2.8	6.5	0.14

Notes: S_{BET}: specific surface area; $V_{pore,t}$: total pore volume; D_{ave}: average pore size; Ni_{dis}: Ni dispersion measured by H_2 chemisorption; TOF_{ini}: initial TOF for the dehydrogenation of 1,2-cyclohexanediol calculated at 250 °C of reaction temperature and 160 h^{-1} of liquid hourly space velocity (LHSV). [a] 2 wt% of sodium sulfate is added as promoter.

Fig. 6 shows the bright-field TEM images of Si–20Ni(*Y*) catalysts prepared at G-D–P time equal to 4 and 24 h, to study the change of morphology of the as-prepared catalysts. Generally, nickel phyllosilicate is prepared by the basification of nickel salt onto a silica surface under a hydrothermal condition.[16,24,41] In a basic aqueous solution, nickel salt forms the nickel hydroxide species, which subsequently react with silicic acid to generate nickel phyllosilicate through a heterocondensation/polymerization reaction.[41] Kim *et al*. reported the Pd@SiO_2-Niphy nanostructure prepared *via* this formation mechanism,[55] over which needle-like, branched nickel phyllosilicates were formed by the dissolution of a nickel salt and the simultaneous condensation with the SiO_2 shell of the core–shell Pd@SiO_2 nanoparticle. Park *et al*. prepared a nickel phyllosilicate/SiO_2 nanostructure by the hydrothermal treatment of a core–shell Ni@SiO_2 nanoparticle.[16] The generated nickel phyllosilicate layer also exhibited a needlelike branched morphology, and was anchored on the outside surface of the nanostructure.[16] In the present work, as discussed in the IR and XRD analyses above, over the Si–20Ni(*Y*) catalysts, nickel phyllosilicates increase in concentration with increasing the G-D–P time. In the present figure, one can see that, some nano-sized spherical particles with needle-like branches exist on both the images of Si–20Ni(4) and that of Si–20Ni(24), which can be distinguished due to the high density of nickel phyllosilicate compared to that of silica.[55] These branches are *ca*. 5–30 nm in length and 1–2 nm in thickness. Moreover, it is found that, more needle-like branches are observed clearly over Si–20Ni(24) than over Si–20Ni(4). In addition, these generated branched nickel phyllosilicates are mainly distributed over the edges of the nanoparticles (see the red ring in Fig. 6 ii-2). Thus, we proposed that the generated nickel phyllosilicates are mainly located on the external surface of the nanoparticles. The XPS results support this assumption (see ESI Fig. 1S†). With increasing the G-D–P time, the mean diameter of the nanoparticles increases from *ca*. 25 to *ca*. 35 nm (see ESI Fig. 2S†).

Fig. 7 shows the HAADF-STEM images and cross-sectional compositional line profiles of Si–20Ni(*Y*) catalysts, choosing the G-D–P time equal to 4 and 24 h as those in Fig. 6 above, to unambiguously confirm the morphologies and distributions of Si and Ni atoms in the particles of silica–nickel nanoparticles. In Fig. 7 i-1 and 7 ii-1, the bright floccules over the lower contrast spherical particles can be related to the nickel

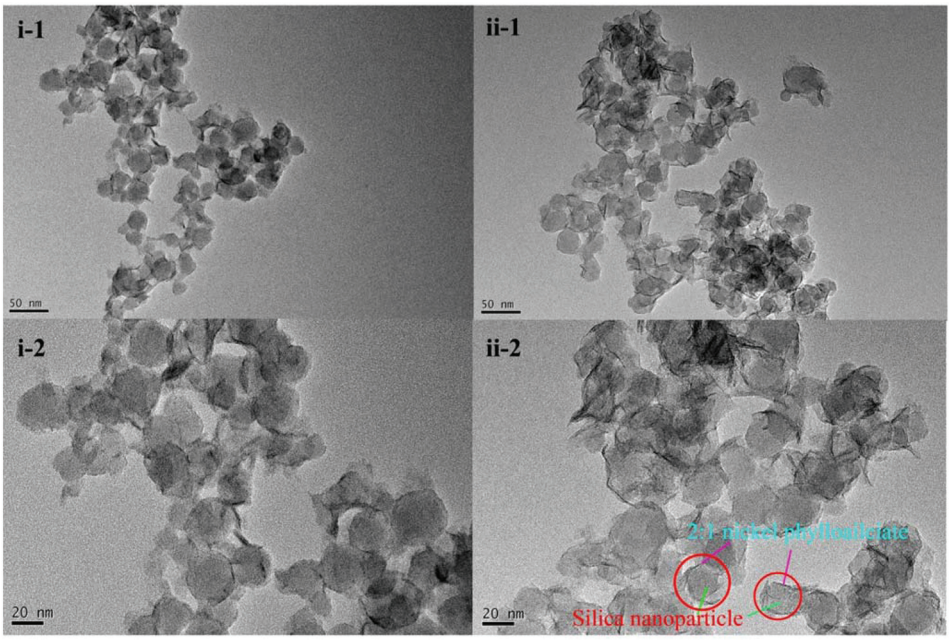

Fig. 6 Bright-field TEM images of Si–20Ni(*Y*) catalysts with different magnification (1 and 2), *Y* = (i) 4 and (ii) 24, respectively; typical embracement effect of nickel phyllosilicates phase around the nanoparticles is observed (for example, see the red rings).

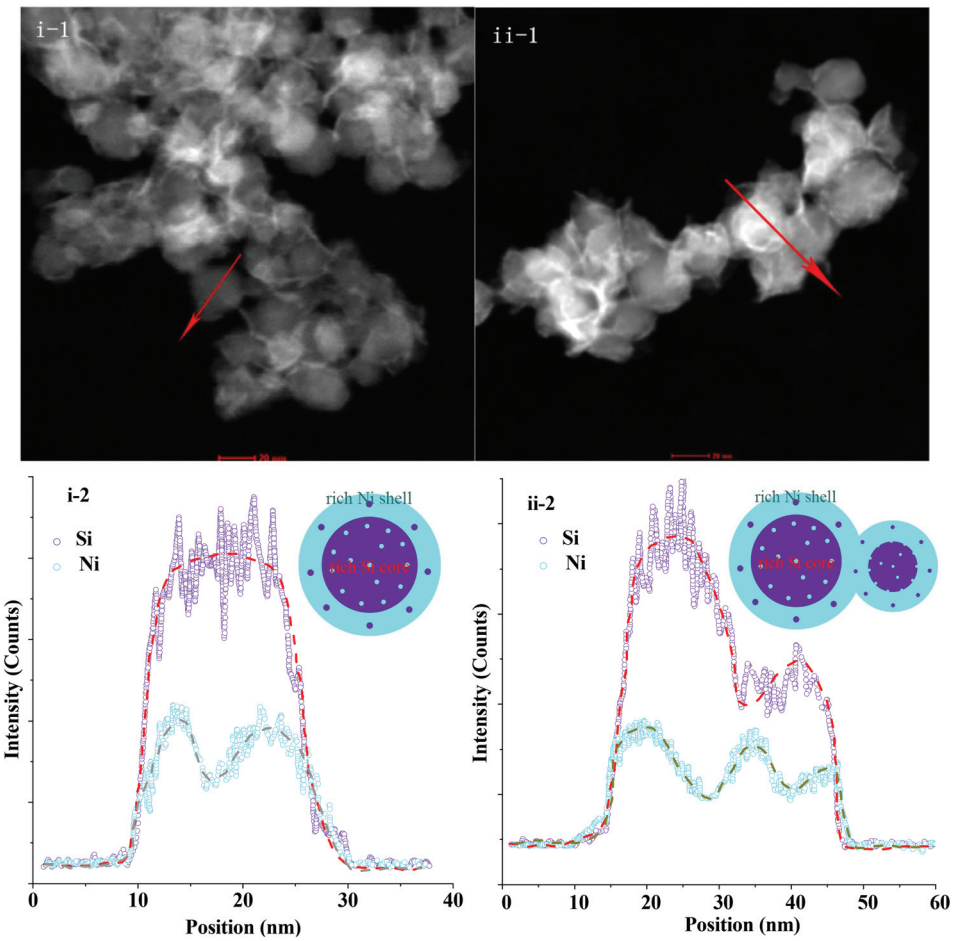

Fig. 7 (1) HAADF-STEM micrographs and (2) cross-sectional compositional line profiles drawn along the row of the bright atomic columns on the nanoparticles of Si–20Ni(*Y*) catalysts, *Y* = (i) 4 and (ii) 24, respectively.

phyllosilicate phase, which refer to the needle-like thin branches observed in the bright-field TEM images (Fig. 6). From the results obtained, more bright floccules are observed over Si–20Ni(24) (Fig. 7 ii-1) than over Si–20Ni(4) (Fig. 7 i-1) due to the increased formation of nickel phyllosilicates with increasing the G-D–P time. This result is in line with the FT-IR, XRD, and TEM analyses above. First, a simply spherical particle with few flocculence-like nickel phyllosilicates in Si–20Ni(4) (Fig. 7 i-1) is chosen to analyze the distributions of Si and Ni atoms by the compositional line profile (Fig. 7 i-2). This nano-sized silica–nickel composite shows a diameter of *ca*. 23 nm. It is interesting to note that, this as-obtained nanoparticle is not separated simply as a pure silica core and a pure nickel species shell, but as a Si-rich core and a Ni-rich shell. Firstly, the existence of the nickel phyllosilicate compound, which includes both silicon and nickel elements, obscures the boundary of the Si-core and Ni-shell. This fact impedes the formation of the pure silica core and nickel species shell. Moreover, during the G-D–P process, the gelation of the colloidal silica solution is remarkably quicker than the deposition–precipitation of nickel. Consequently, during the deposition–precipitation of nickel, some nickel cations probably dip into the pores of the silica particles and are subsequently precipitated in these pores. This also impedes the formation of the pure silica core and nickel species shell. However, in Fig. 7 i-2, the layer at a depth of *ca*. 5 nm from the outermost layer can be assigned to a Ni-rich layer, whereas the distribution of Si is more diffused, proximately in the depths of *ca*. 5–11.5 nm from the outmost layer. Within the nanoparticle, the Ni-rich layer is composed of nickel oxides formed by the decomposition of nickel hydroxides, and nickel phyllosilicates generated mainly during the aging procedure; and the Si-rich layer exists in the form of silica and also nickel phyllosilicates. Nevertheless, this nickel–silica composite is defined as a kind of core–shell-like silica@nickel species nanoparticle.

Moreover, a twin-particle (with diameters equal to *ca*. 22 and 13 nm, respectively) surrounded by obvious flocculent nickel phyllosilicates in Si–20Ni(24) (Fig. 7 ii-1) is selected, and its distributions of Si and Ni atoms are also analyzed *via* the compositional line profile (Fig. 7 ii-2). The result shows that, two maxima in the Si signals are discernible at *ca*. 25 and 41 nm, which can be attributed to the two Si-rich cores of the twin-particle chosen, and three smaller maxima in the Ni signals are observed at *ca*. 20, 34 and 44 nm, which can be assigned to the three Ni-rich shells of the twin-particle. Moreover, this demonstrates that the first particle shows a higher Si/Ni atomic signal ratio than the second one. This result can be explained by the fact that, the first particle possesses a smaller surface/volume ratio than the second one because of its bigger particle size; therefore, it is probable that a thinner layer of Ni is deposited over the former particle than the latter one. Moreover, it is found that, these core–shell-like silica@nickel species nanoparticles are easily deformed, and some dark dots are formed over the surface of the nanoparticles when the electron beam directly irradiates for a long time during the TEM and STEM measurements (see ESI Fig. 3S†). It can be related to the formation of metallic nickel nanoparticles due to the reduction of the Ni species by high energy electrons.[16]

Fig. 8 shows the FE-SEM images of Si–20Ni(4) and reduced Si–20Ni(4) catalysts. The Si–20Ni(4) catalyst (Fig. 8a) shows the spherical shape particles, exhibiting a narrow size distribution of 20–40 nm with an average diameter of *ca*. 30 nm. This observation is consistent with the results obtained in the TEM and HAADF-STEM images. These spherical particles accumulate together, generating the obvious mesoporosity. As discussed above, these mesoporous structures are characterized in the N_2 absorption/desorption isotherms as H1/or H2 type hysteresis loops, which are related to the cylindrical or ink bottle-shaped pore structures. After reduction (Fig. 8b), the spherical particle morphology of Si–20Ni(4) is maintained to a large extent. This suggests that no obvious aggregation and sintering of nickel metal particles are present after the reduction process.

Fig. 9 shows the H_2-TPR profiles of *X*Ni–Si(4), 20Ni–Si(*Y*), and 20Ni–Si(4)–DP catalysts. In the 10Ni–Si(4) catalyst, a much wider range from 300 to 780 °C with an asymmetric peak at 618 °C is observed, which consists of two components with maxima at 475 and 618 °C, respectively. According to previous papers,[24,56] these two peaks are attributed to the reduction of

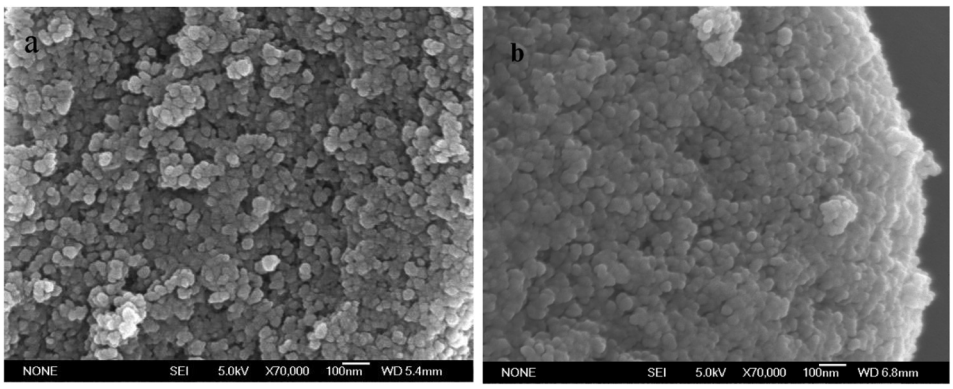

Fig. 8 FE-SEM images of (a) Si–20Ni(4) and (b) reduced Si–20Ni(4) catalysts; reduced temperature = 450 °C (4 h).

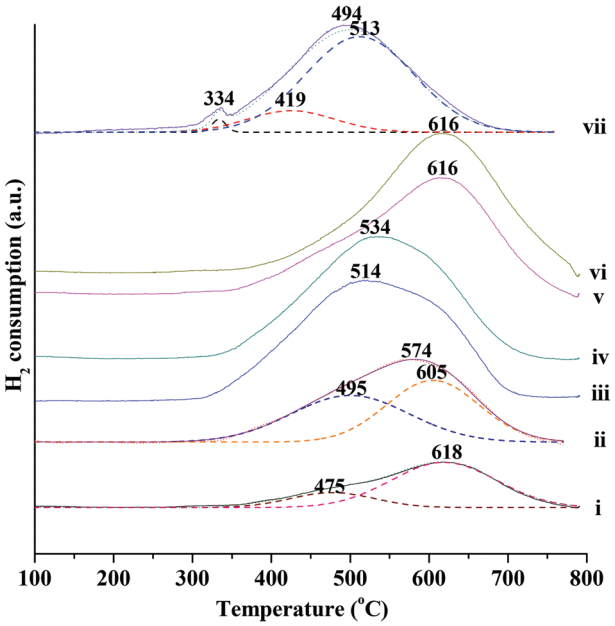

Fig. 9 H_2-TPR profiles of various catalysts: Si–*X*Ni(4), *X* = (i) 10, (ii) 20, and (iii) 50, respectively; 20Ni–Si(*Y*), *Y* = (iv) 2, (v) 12 and (vi) 24, respectively; and (vii) Si–20Ni(4)–DP.

supported nickel oxide (475 °C) and that of nickel phyllosilicate (618 °C), respectively. In the present work, combining the above TEM (Fig. 6) and HAADF-STEM (Fig. 7) analyses, we propose that the peak at 475 °C should be assigned, more accurately, to the nickel oxides in the Ni-rich shells of silica@nickel species nanoparticles, and the peak at 618 °C to the nickel phyllosilicates distributed mainly over the periphery of the silica@nickel species nanoparticles. With increasing Ni loading (Curve i to iii, in order), the main reduction peak shifts to the lower temperature from 618 °C for 10Ni–Si(4) (Curve i) to 514 °C for 50Ni–Si(4) (Curve iii). This finding can be ascribed to the increased concentration of nickel oxides within the silica@nickel species nanoparticles with increasing the Ni loading, in line with the XRD results above.

However, for the 20Ni–Si(*Y*) catalysts, with increasing G-D–P time (Curve iv, ii, v, vi, in order), the main reduction peak shifts obviously to the higher temperature, from 534 °C for 20Ni–Si(2) to 616 °C for 20Ni–Si(24). As confirmed by FT-IR and XRD analyses, nickel phyllosilicates increase in amount with increasing the G-D–P time. Moreover, it is known that[24] a supported nickel phyllosilicate is more difficult to reduce than unsupported ones. Furthermore, the nickel species are reduced at a higher temperature due to the interaction with the support, as often seen for supported oxides catalysts.[24] In this work, for the 20Ni–Si(*Y*) catalysts, the increased reduction temperature with increasing G-D–P time may be due to both the increase in the formation of nickel phyllosilicates and the enhancement of the interaction between the nickel species and silica support.

Comparatively, the 20Ni–Si(4)–DP catalyst exhibits a peak at 494 °C with a shoulder peak at 334 °C. Typically, pure NiO is characterized by a single TPR peak at 300–400 °C.[56] Hence, the small peak at 334 °C can be attributed to the reduction of free nickel oxide. The peak at 494 °C can be deconvoluted into two peaks at 419 and 513 °C, which may be related to the reduction of nickel oxide and nickel phyllosilicate, respectively. Moreover, one can obtain that, the area ratio between nickel phyllosilicate and nickel oxide over Si–20Ni(4)–DP is clearly higher than that over Si–20Ni(4). This result indicates that the concentration of nickel phyllosilicates in the former catalyst is higher than the latter one, which is in line with the FT-IR and XRD analyses. However, interestingly, the main reduction peak of Si–20Ni(4)–DP (494 °C) is clearly lower than that of Si–20Ni(4) (574 °C), which may be caused by a weaker interaction between the nickel species and the silica support over the former catalyst than the latter one. These results above indicate that, Si–20Ni(4)–DP probably possesses a lower dispersion of nickel, relative to Si–20Ni(4), because of the existence of free nickel oxides and the weak interactions of nickel species and silica support.

3.3. Discussion on the formation of the core–shell-like silica@nickel species nanoparticle

As is well known, silica exhibits its zero charge point at pH value = 3. In the preparation of core–shell-like silica@nickel species nanoparticles, a colloidal silica solution (Na_2O type) with a high pH value (*ca.* 10) is used, well above the zero charge point. Therefore, the silica surface is negatively charged, facilitating the adsorption of nickel cations. Waterborne colloids own a surrounding "cloud" of water and electrolytes, which is called the "double-layer," including a layer of bound counter ions called the Stern layer, and a layer of diffuse cations and anions noted as the Guoy layer.[57] There are two types of water present in a colloidal silica solution called as "bound" water and "free" water. The former is bounded by an electrolyte near the silica surface through hydrogen bonding, inhibiting the gelation of the colloidal silica solution.[57] In a basic aqueous solution, nickel hydroxide is the most stable compound among the nickel aqua species when the temperature ranges from 25 to 100 °C,[16] although nickel phyllosilicate can be also generated *via* precipitation of nickel onto the surface of the silica by basification of the nickel(II) solution.[24] The colloidal silica solution then loses its stability, which is controlled in terms of electrolyte-pH, as a result of aggregation of colloidal particles. During the G-D–P procedure in the present work, nickel nitrates react first with the stabilizer, sodium hydroxide in the solution, generating nickel hydroxides. This fact makes the pH value of solution decrease largely, and thus promotes the aggregation of colloidal silica particles. Moreover, the high level of electrolytes, herein the nickel nitrates, leads to the increase in the rate of coagulation of the colloidal silica particles as a result of the decrease in thickness of the "bound" water layer, resulting in closer approaching particles.[57]

Interestingly, in this work, we can accurately relate these above assumptions to the changes in actual yield of silica loading and pH value *versus* the G-D–P time (see Fig. 1b).

At the beginning of G-D–P process (stage 1), the pH value decreases abruptly from *ca*. 10 to 8. This phenomenon can be due to the consumption of the free stabilizer sodium hydroxides in the solution by nickel nitrates. From stage 1 to 0.4 h of G-D–P (stage 2), the pH value decreases at a quick rate. Hence, the stabilization of the colloidal silica solution is destroyed largely, and the colloidal silica particles aggregate rapidly. One can observe that, the actual yield of gelation of silica increases steeply in this period, and above 96% of colloidal silica solutions are gelled after 0.4 h of G-D–P.

The $[Ni(OH_2)_6]^{2+}$ species exists in a nickel nitrate aqueous solution with a stronger acidity (pK_1 = 6.5–10.2, $I > 0$) than silicic acid.[58,59] In previous literature,[41,51] the nature of the Ni(II) species in silica and siliceous materials supported nickel prepared by the deposition–precipitation (D–P) approach have been investigated systematically. During the D–P of Ni, there is competition between the formation of nickel hydroxide and that of nickel phyllosilicate.[41] Nickel hydroxide is formed through an infinite olation-type condensation of $[Ni(OH)_2(OH_2)_4]^0$ precursors.[24,41,51] Comparatively, nickel phyllosilicate can be generated *via* two different mechanisms[24,41]: One is the deprotonation of aquanickel cations by hydroxide ions, followed by a heterocondensation and polymerization reaction with the silicic species in aqueous solution; the other is a $Ni(OH)_2$ depolymerization/Ni–O–Si heterocondensation/polymerization reaction. In both mechanisms of the generation of nickel phyllosilicate, a prerequisite that should be noted: the silicic species in aqueous solution must be monomeric before the formation of nickel phyllosilicate. Thus, in the preparation of silica supported nickel, the generation of nickel hydroxide is kinetically favored than that of nickel phyllosilicate, especially at high Ni loading.[24,41] It is due to the restriction of the amount of monomeric silicic species in aqueous solution, which is limited to the dissolution of the silica framework.[41] However, at the aging stage, nickel hydroxide can transform into nickel phyllosilicate *via* the second mechanism with the gradual dissolution of the silica framework.

In this work, we provide experimental evidence for the assumptions depicted above. For the Si–*X*Ni(4) catalysts (see Fig. 2 and 4), at relatively low Ni loading, the Ni(II) phase is mainly nickel phyllosilicates, and then with increasing Ni loading, the ratio of nickel hydroxides/nickel phyllosilicates increases, due to the limitation of the dissolution of the silica framework. For the Si–20Ni(*Y*) catalysts (see Fig. 3 and 4), with increasing the G-D–P time, nickel hydroxides are transformed into nickel phyllosilicates because of the gradual dissolution of the silica framework. Moreover, after the dissolution of the silica framework into monomeric silicic species, and the movement of these soluble monomeric silicic species in aqueous solution, it is reasonable to deduce that, the reaction between the depolymerized nickel hydroxides and soluble monomeric silicic species should occur primarily over the interface between the precipitated nickel hydroxides and aqueous solution. The experimental evidence in TEM (Fig. 6) and STEM (Fig. 7) supports this deduction. The needle-like, thin branches in the TEM images and floccules in the STEM images are associated with the nickel phyllosilicates phase. Nickel phyllosilicates are distributed over the outside surface of spherical silica@nickel species nanoparticles, and subsequently embrace them (see the red rings in Fig. 6). Furthermore, the nickel phyllosilicates phase around the silica@nickel species nanoparticles probably brings an effect of segregation among these nanoparticles, thus benefitting the stability and dispersion of nanoparticles. We can see that, in Fig. 8, the morphology of the Si–20Ni(4) nanoparticle is retained to a large extent after the reduction procedure.

We can also associate the experimental results above with the changes of actual yield of Ni loading and pH value *versus* the G-D–P time (see Fig. 1b). One can see that, a plain stage is formed from 0.4 to 2 h of G-D–P when the pH value is equal to *ca*. 5 (stage 3); moreover, the yield of actual Ni loading increases steeply. The formation of the plain stage can be caused by the formation of a dynamic equilibrium between the generation of hydroxide ions by the hydrolysis of urea, and the consumption of hydroxide ions for the formation of nickel hydroxides and nickel phyllosilicates. At 2 h of G-D–P, an actual yield of Ni loading = *ca*. 92% is obtained, and after that, the pH value begins to increase at a relatively mild speed from *ca*. 5 to 8 (stage 4). It is suggested that, this process probably corresponds to the transformation from nickel hydroxides to nickel phyllosilicates with the depolymerization of nickel hydroxides and dissolution of the silica framework,[24] which consumes some hydroxides ions. In addition, at the stage 4, the generation of hydroxide ions seem quicker than its consumption; therefore, the pH value increases mildly. After *ca*. 20 h of G-D–P, the pH value increases abruptly from *ca*. 8 to 10, and then fluctuates around these high values (stage 5). This consequence can be explained by the fact that, at this moment, almost all the nickel hydroxides have been transformed into nickel phyllosilicates, or that the generated nickel phyllosilicates embrace the nanoparticles, and therefore prohibit the further transformation of nickel hydroxides to nickel phyllosilicates. Moreover, the mean diameter of silica@nickel species nanoparticles detected by FE-SEM also changes with the G-D–P time, which can also be well explained (see ESI S2†).

Based on the discussion above, the formation mechanism of core–shell-like silica@nickel species nanoparticles is proposed in Scheme 1, and it is depicted as follows. During the G-D–P procedure, the colloidal silica solution is gelled quickly, and nickel salts are gradually deposited–precipitated over the gelled spherical SiO_2 nanoparticles. At the aging stage, nickel hydroxides transform into nickel phyllosilicates with the dissolution of the silica nanoparticle matrix. However, limited to the dissolution rate of the silica framework, nickel oxides are exhibited as the main Ni phase at the relatively high Ni loading and short G-D–P time, whereas nickel phyllosilicates are the main Ni phase at the relatively low Ni loading and long G-D–P time. After calcination, the core–shell-like silica@nickel species nanoparticles are generated. Moreover, nickel phyllosilicates, with a morphology of needle-like branches observed in the TEM images and a morphology of floccules seen in the

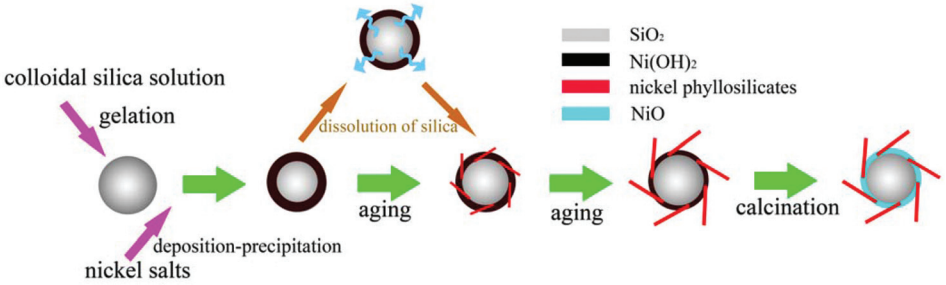

Scheme 1 Proposed mechanism for the preparation of core–shell-like silica@nickel species nanoparticle by the G-D–P approach.

STEM images, are formed over the outside of core–shell-like silica@nickel species nanoparticles, and subsequently enwrap the nanoparticles.

3.4. Catalytic dehydrogenation of 1,2-cyclohexanediol to catechol

For the dehydrogenation of 1,2-cyclohexanediol to catechol, in addition to the aimed catechol, the main byproducts are phenol and *o*-hydroxyl-cyclohexanone. In our previous work,[29] we studied systematically the reaction mechanism and the role of the Na promoter for the dehydrogenation of 1,2-cyclohexanediol to catechol over a nickel-based catalyst. The results obtained exhibited that,[29] catechol was generated over the Na-modified Ni metal complexity, *o*-hydroxyl-cyclohexanone was an important reaction intermediate formed on the unreduced or reduced Ni, and phenol, as the main byproduct, was concerned with the pyrolysis of catechol. In the present work, the core–shell-like silica@nickel species nanoparticles prepared by G-D–P and the contrastive nickel-based catalyst prepared by conventional D–P have been used as catalysts for the dehydrogenation of 1,2-cyclohexanediol to catechol. Before the reactions, 2 wt% of Na is added into the catalysts as the promoter, and all the catalysts are uniformly reduced by hydrogen at 450 °C for 4 h.[29]

Fig. 10 shows the effect of Ni loading on the catalytic properties of 2Na/Si–*X*Ni(4) catalysts (X = 10–50). With an increase in the Ni loading, the conversion increases firstly, and then changes very slightly, retaining a high value above 99.9% when the Ni loading is higher than 10 wt%. Moreover, when the Ni loading increases, the selectivity of catechol demonstrates first an increase, attaining its maximum *ca*. 94.4% at 20 wt% of Ni loading, and then it decreases. Comparatively, the selectivities of *o*-hydroxyl-cyclohexanone and phenol show very low values (<0.5%) when the Ni loading is below 30 wt%. However, they increase dramatically when the Ni loading is above 30 wt%. This consequence can be caused by the aggregation and agglomeration of the nickel species particles at the relatively high Ni loading, which is probably unfavorable for the main reaction, but accelerates the formation of byproducts. Anyway, there exists an optimal Ni loading for the dehydrogenation of 1,2-cyclohexanediol at *ca*. 20 wt%.

The dispersions of metallic nickel and initial surface-atom-based reaction rates (turnover frequencies, TOF) of various catalysts are shown in Table 1. First, it is found that, the metallic nickel dispersion decreases with increasing the Ni loading, from 20.7% for Si–10Ni(4) to 7.0% for Si–50Ni(4). This can be due to the aggregation or agglomeration of the nickel species particles at the high loading of nickel. However, it is interesting for the Si–20Ni(Y) catalysts that, with increasing the G-D–P time, the dispersion of metallic nickel decreases firstly and obtains its minimum at 4 h of G-D–P time (10.7%), followed by a monotonic increase after 4 h of G-D–P time. As discussed in Fig. 1b above, more than 98.6% of the colloidal silica solution has been gelled at G-D–P time >1 h. However, only 68.2% and 92.0% of nickel are deposited–precipitated at 1 and 2 h of G-D–P time, respectively, and more than 99% yields of deposition–precipitation of nickel are obtained only after 4 h of G-D–P time. According to the FT-IR, XRD, and TEM results above, nickel phyllosilicates are formed mainly during the aging period, which envelope the core–shell-like silica@nickel species nanoparticles and increase in concentration with increase in G-D–P time. Based on these conclusions, it is obtained that, (1) Si–20Ni(1) and Si–20Ni(2) catalysts have a higher dispersion of metallic nickel than Si–20Ni(4), which is probably due to the lower actual Ni loadings over the former two catalysts than the latter one; (2) after 4 h of G-D–P, the dis-

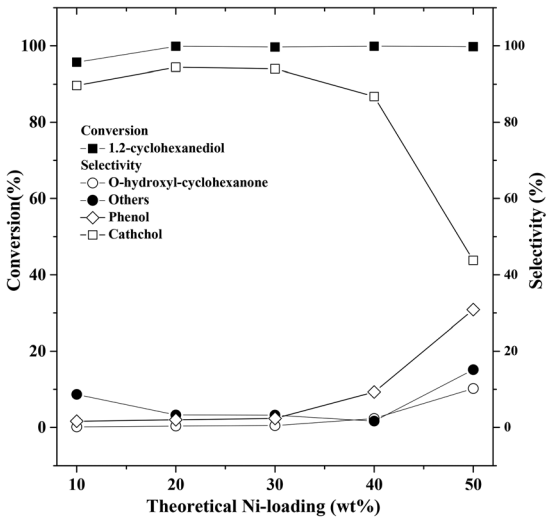

Fig. 10 Catalytic performances of 2Na/Si–*X*Ni(4) catalysts as a function of X (X = 10–50); reduction temperature = 450 °C, reaction temperature = 320 °C, LHSV = 1.42 h^{-1}.

persion of metallic nickel increases with increasing the G-D–P time, which can be related to the increase in the formation of nickel phyllosilicates. This result proves that, the nickel phyllosilicate layers formed during the G-D–P procedure is beneficial to the dispersion of nickel, because they distribute over the periphery of the core–shell-like silica@nickel species nanoparticles, and therefore bring an effect of segregation among the nanoparticles. Moreover, the dispersion of metallic nickel of Si–20Ni(4)–DP is also present in Table 1, which shows an obviously lower dispersion of metallic nickel (6.5%) than that of Si–20Ni(4) (10.7%). This result suggests that the catalyst prepared by the G-D–P method depicted in this work owns a higher dispersion of metallic nickel than that prepared by the conventional D–P method.

Moreover, the initial TOF values are normalized by the number of exposed surface metallic nickel atoms measured by H_2 chemisorption uptake before the catalytic measurements. The conversion of the reaction is controlled, especially in the range of 4%–13% for ensuring the experimental results are obtained in the intrinsic kinetics region. Here, four Si–20Ni(Y) catalysts (Y = 2, 4, 12, and 24) are tested. The catalyst weight (10–20 mg) adopted is based on the same amount of surface metallic nickel atoms = 9.9×10^{17}. Then, an important conclusion can be drawn that, the initial TOF value over the surface reduced nickel metal atoms increases with the dispersion of metallic nickel. One can also see that, the TOF value for 2Na/Si–20Ni(4) (0.22 h^{-1}) is obviously higher than that for 2Na/Si–20Ni(4)–DP (0.14 h^{-1}), indicating the higher catalytic efficiency of the former catalyst than the latter one. These results also indicate that the dehydrogenation of 1,2-cyclohexanediol to catechol over Na-doped nickel catalysts is a structurally sensitive reaction.[60] For this catalytic reaction, the coordinately unsaturated surface metallic nickel atoms are more active than those in the low-index surface planes predominately exposed on larger nickel crystallites.

The comparison of the catalytic property of the 2Na/Si–20Ni(4) catalyst prepared by G-D–P and the 2Na/Si–20Ni(4)–DP catalyst prepared by conventional D–P is studied. As shown in Fig. 11, the 2Na/Si–20Ni(4) catalyst has an obviously better catalytic performance than the 2Na/Si–20Ni(4)–DP catalyst in the addressed reaction. For 2Na/Si–20Ni(4), the conversion of reactant can be maintained stably at above 99.9% within 300 h, followed by a slight decrease to 98.8% after 432 h. The catechol selectivity achieves its maximum at 98.5% after an upward tendency within the first 200 h, and then it decreases gradually to below 90% after 324 h. As a result, the high performance with a yield of aimed catechol above 90% can be obtained for as long as 324 h of on-stream reaction. In comparison, for 2Na/Si–20Ni(4)–DP, a lower catechol selectivity at 90.5% is obtained at 31 h. Furthermore, a severe loss of activity (<80%) is observed after only 100 h of time on-stream. As discussed above, the dispersion of metallic nickel over Si–20Ni(4) is higher than that over Si–20Ni(4)–DP. Moreover, it has been proposed in previous studies that,[22,46,61] the formation of hard-reducible metal silicates contributes largely to the stability of metal supported catalysts. In this work, for the 2Na/Si–20Ni(4) catalyst prepared by the G-D–P approach, the better selectivity toward the aimed product catechol and the better stability for the model reaction can be explained by the higher dispersion of metallic nickel over the special core–shell-like silica@nickel species nanoparticles stabilized by outer nickel phyllosilicates layers. In addition, we can compare the Si–20Ni(4) catalyst prepared by the G-D–P approach described in this paper with the Si–20Ni(4)–DP catalyst prepared by conventional D–P approach. As shown in the IR (Fig. 3) and XRD (Fig. 2) results above, the nickel phyllosilicates over Si–20Ni(4)–DP are more than Si–20Ni(4) in concentration. However, in the H_2-TPR profiles (Fig. 9), we find the existence of free nickel oxide compounds and weak interactions between nickel species and silica support over the Si–20Ni(4)–DP catalyst. As a result, the dispersion of metallic nickel over the Si–20Ni(4)–DP catalyst is clearly lower than the Si–20Ni(4) catalyst (Table 1). This result suggests that, the G-D–P method provides an effective approach for preparing highly dispersed and stable catalysts. It is also reasonable to deduce that, the highly dispersed nickel species is necessitated for obtaining optimum performance in the dehydrogenation of 1,2-cyclohexanediol to catechol.

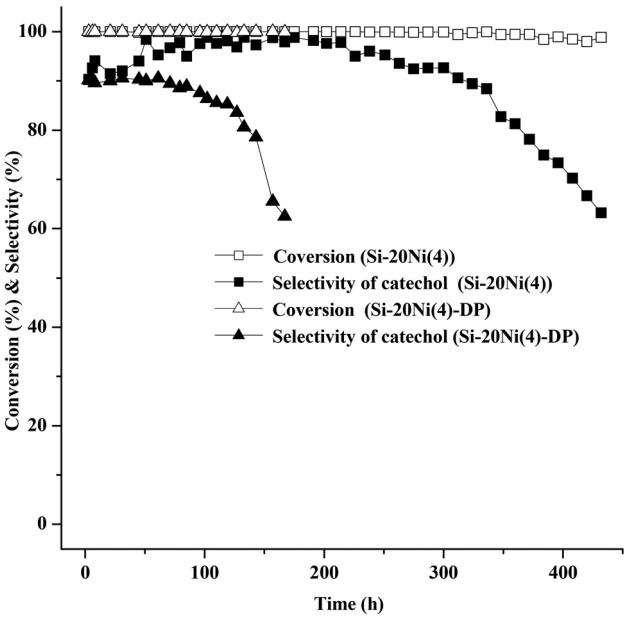

Fig. 11 Catalytic performance of 2Na/Si–20Ni(4) catalyst as a function of time on stream (TOS); reduction temperature = 450 °C, reaction temperature = 320 °C, LHSV = 1.42 h^{-1}.

4. Conclusions

A simple approach named the gel-deposition–precipitation (G-D–P) approach is developed to prepare core–shell-like silica@nickel species nanoparticles using a commercial grade colloidal silica solution directly as the source of silica cores. The core–shell-like silica@nickel species nanoparticles can serve as a highly dispersed and stable catalyst. This approach can be readily extended to the production of other similar catalyst

systems forming metal phyllosilicates, *e.g.*, core–shell structural silica@cobalt species, @magnesium species, @copper species and @zinc species nanoparticles. During the preparation of silica@nickel species nanoparticles, nickel phyllosilicates are generated mainly during the aging stage because of the interaction between the monomeric silicic species, generated from the gradual dissolution of the silica frameworks, and the depolymerized nickel hydroxides, according to a mechanism of Ni-$(OH)_2$ depolymerization/Ni–O–Si heterocondensation/polymerization. These formed nickel phyllosilicates are distributed over the periphery of the spherical silica@nickel species nanoparticles, thus inhibiting effectively the agglomeration and aggregation of nanoparticles and facilitating the distribution of the nickel species. It favors the applications of silica@nickel species nanoparticles in the field of catalysis. In addition, the preparation (G-D–P) time can be used conventionally to regulate the dispersion degree of nickel over the catalysts prepared by the G-D–P approach, by regulating the formation content of nickel phyllosilicates. Therefore, it can be used easily for detection in structurally sensitive reactions.

Acknowledgements

We are grateful for the financial support from the Project #21376068 for National Natural Science Foundation (NSFC), Program for Lotus Scholar in Hunan Province, and also, Program for Innovative Research Team (Hunan University: IRT1238) of MOE, China.

References

1 M. Valden, X. Lai and D. W. Goodman, *Science*, 1998, **281**, 1647–1650.
2 A. L. Nogueira, R. A. F. Machado, A. Z. de Souza, F. Martinello, C. V. Franco and G. B. Dutra, *Ind. Eng. Chem. Res.*, 2014, **53**, 3426–3434.
3 Z. Wu, Z. Li, G. Wu, L. Wang, S. Lu, L. Wang, H. Wan and G. Guan, *Ind. Eng. Chem. Res.*, 2014, **53**, 3040–3046.
4 R. Narayanan and M. A. El-Sayed, *J. Am. Chem. Soc.*, 2004, **126**, 7194–7195.
5 A. S. Eppler, G. Rupprechter, L. Guczi and G. A. Somorjai, *J. Phys. Chem. B*, 1997, **101**, 9973–9977.
6 C. Harding, V. Habibpour, S. Kunz, A. N.-S. Farnbacher, U. Heiz, B. Yoon and U. Landman, *J. Am. Chem. Soc.*, 2009, **131**, 538–548.
7 M. Chen and D. Goodman, *Science*, 2004, **306**, 252–255.
8 Z. Huang, F. Cui, J. Xue, J. Zuo, J. Chen and C. Xia, *J. Phys. Chem. C*, 2010, **114**, 16104–16113.
9 A. T. Bell, *Science*, 2003, **299**, 1688–1691.
10 J. Lee, J. C. Park, J. U. Bang and H. Song, *Chem. Mater.*, 2008, **20**, 5839–5844.
11 D. J. Sprouster, R. Giulian, L. L. Araujo, P. Kluth, B. Johannessen, N. Kirby and M. C. Ridgway, *J. Appl. Phys.*, 2011, **109**, 113517.
12 H.-Y. Chuang and D.-H. Chen, *Nanotechnology*, 2009, **20**, 105704.
13 K.-M. Kang, H.-W. Kim, I.-W. Shim and H.-Y. Kwak, *Fuel Process. Technol.*, 2011, **92**, 1236–1243.
14 K. Maeda, K. Teramura, D. Lu, N. Saito, Y. Inoue and K. Domen, *J. Phys. Chem. C*, 2007, **111**, 7554–7560.
15 J. Zhai, X. Tao, Y. Pu, X.-F. Zeng and J.-F. Chen, *Appl. Surf. Sci.*, 2010, **257**, 393–397.
16 J. C. Park, H. J. Lee, J. U. Bang, K. H. Park and H. Song, *Chem. Commun.*, 2009, 7345–7347.
17 S. H. Joo, J. Y. Park, C.-K. Tsung, Y. Yamada, P. Yang and G. A. Somorjai, *Nat. Mater.*, 2009, **8**, 126–131.
18 Z. Li, L. Mo, Y. Kathiraser and S. Kawi, *ACS Catal.*, 2014, **4**, 1526–1536.
19 Z. Libor and Q. Zhang, *Mater. Chem. Phys.*, 2009, **114**, 902–907.
20 P. Reiss, M. Protière and L. Li, *Small*, 2009, **5**, 154–168.
21 H. E. Bergna, *The colloid chemistry of silica*, American Chemical Society, Washington, DC (United States), 1994.
22 P. Jin, Q. Chen, L. Hao, R. Tian, L. Zhang and L. Wang, *J. Phys. Chem. B*, 2004, **108**, 6311–6314.
23 D. A. Ward and E. I. Ko, *Ind. Eng. Chem. Res.*, 1995, **34**, 421–433.
24 P. Burattin, M. Che and C. Louis, *J. Phys. Chem. B*, 1997, **101**, 7060–7074.
25 G. Dıaz, R. Perez-Hernandez, A. Gomez-Cortes, M. Benaissa, R. Mariscal and J. Fierro, *J. Catal.*, 1999, **187**, 1–14.
26 Y. Zuo, W. Song, C. Dai, Y. He, M. Wang, X. Wang and X. Guo, *Appl. Catal., A*, 2013, **453**, 272–279.
27 A. Yu. D'yaKonov, V. D. Stytsenko, S. A. Nizova, P. S. Belov and A. Y. Rozovskii, *Kinet. Catal.*, 1984, **25**, 409–411.
28 Y. Zuo, W. Song, C. Dai, Y. He, M. Wang, X. Wang and X. Guo, *Appl. Catal., A*, 2013, **453**, 272–279.
29 B.-H. Chen, C. Huang, D.-G. Huang, C.-W. Luo, H.-T. Li and Z.-S. Chao, *Appl. Catal., A*, 2014, **470**, 239–249.
30 H. Nagahara, M. Ono, M. Konishi and Y. Fukuoka, *Appl. Surf. Sci.*, 1997, **121–122**, 448–451.
31 Y. Usui, K. Sato and M. Tanaka, *Angew. Chem., Int. Ed.*, 2003, **42**, 5623–5625.
32 B. P. C. Hereijgers, R. F. Parton and B. M. Weckhuysen, *ACS Catal.*, 2011, **1**, 1183–1192.
33 P. J. Cordeiro, P. Guillo, C. S. Spanjers, J. W. Chang, M. I. Lipschutz, M. E. Fasulo, R. M. Rioux and T. D. Tilley, *ACS Catal.*, 2013, **3**, 2269–2279.
34 K. Na, C. Jo, J. Kim, W.-S. Ahn and R. Ryoo, *ACS Catal.*, 2011, **1**, 901–907.
35 C. Antonetti, A. M. R. Galletti, P. Accorinti, S. Alini, P. Babini, K. Raabova, E. Rozhko, A. Caldarelli, P. Righi, F. Cavani and P. Concepcion, *Appl. Catal., A*, 2013, **466**, 21–31.
36 Q. Yang, X. Yang, Y. Wang, H. Wang and Q. Cheng, *Res. Chem. Intermed.*, 2012, **38**, 2277–2284.
37 Y. Wen, X. Wang, H. Wei, B. Li, P. Jin and L. Li, *Green Chem.*, 2012, **14**, 2868–2875.
38 S. Pei, L. Lin and C. Zeng, *Petro. Technol. (in Chinese)*, 2010, **2**, 146–150.
39 X. Zhu, M. Shen, L. L. Lobban and R. G. Mallinson, *J. Catal.*, 2011, **278**, 123–132.

40 G. Jacobs, P. M. Patterson, Y. Zhang, T. Das, J. Li and B. H. Davis, *Appl. Catal., A*, 2002, **233**, 215–226.
41 P. Burattin, M. Che and C. Louis, *J. Phys. Chem. B*, 1998, **102**, 2722–2732.
42 P. Innocenzi, *J. Non-Cryst. Solids*, 2003, **316**, 309–319.
43 J. Hernández-Torres and A. Mendoza-Galván, *J. Non-Cryst. Solids*, 2005, **351**, 2029–2035.
44 M. Kermarec, J. Y. Carriat, P. Burattin, M. Che and A. Decarreau, *J. Phys. Chem.*, 1994, **98**, 12008–12017.
45 P. Gérard and A. Herbillon, *Clays Clay Miner.*, 1983, **31**, 143–151.
46 Z. Huang, F. Cui, H. Kang, J. Chen, X. Zhang and C. Xia, *Chem. Mater.*, 2008, **20**, 5090–5099.
47 G. Onori and A. Santucci, *J. Phys. Chem.*, 1993, **97**, 5430–5434.
48 M. Casu, A. Lai, A. Musinu, G. Piccaluga, S. Solinas, S. Bruni, F. Cariati and E. Beretta, *J. Mater. Sci.*, 2001, **36**, 3731–3735.
49 H. Liu, H. Wang, J. Shen, Y. Sun and Z. Liu, *Appl. Catal., A*, 2008, **337**, 138–147.
50 Y. Wei, J. Xu, H. Dong, J. H. Dong, K. Qiu and S. A. Jansen-Varnum, *Chem. Mater.*, 1999, **11**, 2023–2029.
51 R. Nares, J. Ramírez, A. Gutiérrez-Alejandre, C. Louis and T. Klimova, *J. Phys. Chem. B*, 2002, **106**, 13287–13293.
52 P. L. Llewellyn, Y. Grillet, F. Schüth, H. Reichert and K. K. Unger, *Microporous Mater.*, 1994, **3**, 345–349.
53 A. E. Sommer Marquez, D. A. Lerner, G. Fetter, P. Bosch, D. Tichit and E. Palomares, *Dalton Trans.*, 2014, **43**, 10521–10528.
54 G. Leofanti, M. Padovan, G. Tozzola and B. Venturelli, *Catal. Today*, 1998, **41**, 207–219.
55 M. Kim, J. C. Park, A. Kim, K. H. Park and H. Song, *Langmuir*, 2012, **28**, 6441–6447.
56 S. Tomiyama, R. Takahashi, S. Sato, T. Sodesawa and S. Yoshida, *Appl. Catal., A*, 2003, **241**, 349–361.
57 H. E. Bergna and W. O. Roberts, *Colloidal silica: fundamentals and applications*, CRC, 2005.
58 J. Burgess, *Metal ions in solution*, Ellis Horwood Chichester, England, 1978.
59 T. Mizutani, Y. Fukushima, A. Okada and O. Kamigaito, *Bull. Chem. Soc. Jpn.*, 1990, **63**, 2094–2098.
60 R. A. Van Santen, *Acc. Chem. Res.*, 2009, **42**, 57–66.
61 T. Toupance, M. Kermarec and C. Louis, *J. Phys. Chem. B*, 2000, **104**, 965–972.

